Evaluation of bimodal microstructures in selective-laser-melted and heat-treated Ti-6Al-4V

Tom McKenna [a,d], Charles Tomonto [b], Greg Duggan [c], Eoin Lalor [c], Seamus O'Shaughnessy [a], Daniel Trimble [a,d],*

[a] Trinity College Dublin, The University of Dublin, Department of Mechanical, Manufacturing and Biomedical Engineering, Parsons Building, Dublin 2, Ireland
[b] 3D Printing Innovation & Customer Solutions, Johnson & Johnson Services Inc., Miami, FL 33126, USA
[c] DePuy Synthes, Loughbeg, Ringaskiddy, Co. Cork P43 ED82, Ireland
[d] AMBER, the SFI Research Centre for Advanced Materials and BioEngineering Research, Ireland

HIGHLIGHTS

- The response of SLM Ti64 to 'cyclical' heat treatment strategies was characterised in terms of microstructure and mechanical performance
- The number of thermal cycles experienced in a 'cyclical' profile heat treatment significantly influences the high-cycle fatigue behaviour
- A lamellar microstructure was shown to out-perform a bimodal microstructure in both tensile and high-cycle fatigue testing.

GRAPHICAL ABSTRACT
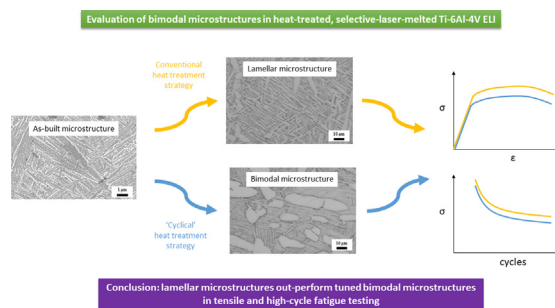
ABSTRACT

As-built, SLM-printed Ti-6Al-4V parts suffer from non-equilibrium, brittle microstructures due to the formation of metastable α′-phase martensite as a result of the printing process. Post-processing heat treatments are required to alleviate residual stress and decompose the martensite into equilibrium phases. Using unconventional 'cyclical' heat treatment profiles, it is possible to achieve a bimodal microstructure as opposed to a more typical lamellar microstructure achieved using conventional heat treatment profiles. In the present research, the effect of cyclical heat treatment parameters (maximum temperature, minimum temperature, number of cycles and cooling regime) on the grain morphology, phase composition and mechanical performance (static and dynamic) has been evaluated. Furthermore, a comparison to a typical lamellar microstructure has been completed as a reference.

© 2023 The Author(s). Published by Elsevier Ltd. This is an open access article under the CC BY license (http://creativecommons.org/licenses/by/4.0/).

1. Introduction

Selective laser melting (SLM) is a metal additive manufacturing process. As a powder bed fusion technology, SLM 'builds' a part up by selectively melting successive and stacked layers of metal powder substrate. Among the suitable titanium-based materials being processed by SLM systems, grade 5 (Ti-6Al-4V) and grade 23 (Ti-6Al-4V ELI) titanium continue to be heavily researched [1]. Grade 23 titanium offers excellent biocompatibility, good endurance strength, reasonable ductility and a relatively low elastic modulus—all of which make this material a popular choice for aerospace, automotive and medical device applications [2].

In the as-printed state, SLM'd grade 23 parts suffer from non-equilibrium, brittle microstructures which often do not conform to standard specifications (e.g. ASTM F3001 standard [3]) for use

---

in service applications. Printed parts often exhibit tensile strengths in excess of 1000 MPa with accompanying ductility values of less than 10 % [4–9]. This can be largely attributed to the martensitic (principally α'-phase) microstructure rendered in the as-built state. Such non-equilibrium microstructure formations are a consequence of the steep thermal gradients, in the order of 10^4–10^6 °C/s^1 [10–12], experienced by the material locally in the wake of each laser scanning vector.

In attempting to address some of the issues of as-built Ti-6Al-4V material, many researchers in the space have employed post-processing heat treatments such as annealing or hot isostatic pressing. Heat treatments for printed Ti-6Al-4V components are designed to alleviate residual stress and decompose the metastable martensite into equilibrium phases while also attempting to tailor the evolving microstructural and mechanical properties [7,9,13–17]. More recently, a small number of research groups [18–21] have developed multi-stage or 'cyclical' heat treatment profiles which have rendered printed Ti-6Al-4V components with unusual microstructure morphologies. The equiaxed or bimodal morphologies achieved in these studies are distinct from the typical lamellar morphologies which evolve in printed Ti-6Al-4V material exposed to more conventional annealing treatment profiles.

Funch et al. [18] transformed an as-built Ti-6Al-4V microstructure into a so-called 'bi-lamellar' microstructure which consisted of large, lamellar α-phase grain surrounded by a fine-grained, dual phase matrix. The authors explored a range of heat treatment steps (β homogenisation step; annealing step; ageing step) which produced a gamut of bi-lamellar microstructures. They found that a β-phase homogenisation step produced a more homogenous microstructure but the tensile test performance suffered as a result. They ultimately only compared the tensile test performance and hardness of two bi-lamellar microstructure samples which offered a very limited view of the mechanical ability of these microstructures. UTS values of approximately 1050 MPa and fracture strain values of within 12.5 % were achieved by one of their bi-lamellar samples.

Sabban et al. [19] implemented a cyclical heat treatment profile which rendered parts with a bimodal microstructure and displayed UTS and fracture strain values of 1000 MPa and 17 %, respectively. However, the authors did not attempt to tune their cyclical treatment parameters, choosing to explore only one treatment strategy. Neither did they compare the mechanical performance of SLM'd parts which experienced a conventional annealing treatment for reference.

Bai et al. [20] researched a cyclical treatment strategy which was effectively identical to that which was designed by Sabban et al. [19]. They reported the cyclically-treated sample to possess a higher mean UTS value, of approximately 1200 MPa, which was as strong as the as-SLM'd material, but it offered poor ductility values at around 10 %. A printed Ti-6Al-4V sample which experienced a standard anneal at 950 °C for 2 h and an air cool achieved a mean UTS of within 900 MPa and a mean ductility of 12 % in this study. The authors also provided evidence that the conventional annealing treatment rendered printed parts with a higher fracture toughness than equivalent parts which were exposed to the cyclical heat treatment strategy.

The heat treatment parameters which could serve to tune bimodal microstructure morphologies, and thus the mechanical performance in printed Ti-6Al-4V parts, have not been fully explored to date. As outlined in preceding paragraphs, there was a wide spectrum of reported static tensile properties for the bimodal morphologies. UTS values ranged 1000–1200 MPa while ductility values measured 10–17 %. In none of the discussed studies were the bimodal microstructures mechanically tested against lamellar counterparts.

Furthermore, there has been no published work done to evaluate the high-cycle fatigue (HCF) performance of bimodal microstructures in printed Ti-6Al-4V parts. The question of whether lamellar or bimodal microstructures exhibit superior HCF in wrought Ti-6Al-4V is contested. Hines et al. [22] and Nalla et al. [23] reported that lamellar microstructures out-performed bimodal microstructures in HCF testing while Zuo et al. [24], Wu et al. [25] and Crupi et al. [26] published evidence to the contrary.

This study seeks to provide broad illumination in to cyclical-profile heat treatments as they are applied to SLM'd grade 23 titanium. The impact of altering cyclical-profile heat treatment variables upon microstructure morphology is investigated. The tensile and HCF performance of various bimodal microstructures and a lamellar reference microstructure is evaluated.

2. Experimental methodology

2.1. Printing of parts

Cylindrical samples (52 mm height; 8 mm diameter) from grade 23 titanium powder on an EOS M290 system at Johnson & Johnson's 3-D Printing Centre of Excellence located in DePuy Synthes (Co. Cork, Ireland). Components were printed vertically, in parallel to the build direction. The SLM process parameters are presented in Table 1. The printed parts measured 99.5 % ± 0.04 % dense using the Archimedes' method.

2.2. Heat treatment of parts

Treatments were conducted in a Carbolite Gero CWF 12/5 laboratory chamber furnace fitted with a Eurotherm Nanodac controller. The generic profile of a cyclical heat treatment is illustrated in Fig. 1, with three cycles depicted. In this study the maximum cycle temperature ($T_{max.}$), the minimum cycle temperature ($T_{min.}$) and the number of cycles experienced were varied. Parts were ramped to $T_{max.}$ at a fixed rate of 5 °C/min before being successively cycled between the $T_{max.}$ and $T_{min.}$ values. Between T_{max} and T_{min} a fixed period heating/cooling rate of 2 °C/min was applied. After a programmed number of cycles had been completed, samples were air-cooled from T_{max} down to atmospheric conditions.

2.3. Tensile testing

Tensile specimens were prepared according to the ASTM E8 cylindrical tensile specimen 4 specification (4 mm gauge diameter; 16 mm gauge length). An axial extensometer (Epsilon model 3442) was attached to each specimen for the duration of each test—until failure—for accurate measurement of engineering strain. Testing was conducted on an Instron 8801 system running Instron Bluehill

Table 1
Pertinent SLM process parameters used to print the samples for this study.

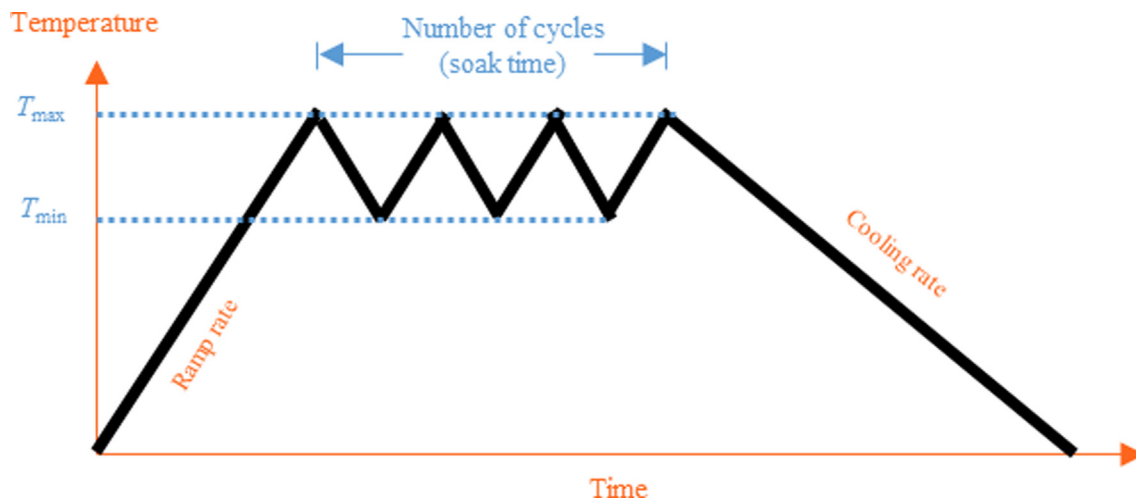| Contour scan laser power (W)	Contour scan scanning speed (mm/s^1)	Infill scan laser power (W)	Infill scan scanning speed (mm/s^1)	Layer thickness (μm)	Hatch distance (μm)	Beam diameter (μm)
190	1250	340	1250	60	120	100

Fig. 1. Illustration of a cyclical heat treatment profile, with the treatment parameters labelled. This instance shows three thermal cycles.

software. The strain rate was set to 2.3 %/min until 6 % strain was achieved, after which a constant strain rate of 6 %/min prevailed until failure occurred. Values for engineering ultimate tensile stress (UTS) and engineering fracture strain—and not true stress nor true strain—are reported in this work. The reader is referred to recent work by Huang et al. [27] which presents both true and engineering fracture strain data of SLM'd Ti-6Al-4V for comparison. Furthermore, each tensile test data figure produced is the mean value calculated from three tests accompanied by the calculated standard error for each sample.

2.4. Fatigue testing

As the achievable fracture toughness values are relatively low in titanium alloys [2], the crack initiation phase contributes extensively to the overall fatigue life when cycling at stress amplitudes close to the endurance limit [28]. Therefore, the production of Ti-6Al-4V parts with microstructures which maximise the exhibited fatigue strength is highly desirable.

Fatigue testing was conducted with specimens adhering to ASTM E466 using Instron WaveMatrix software on an Instron 8801 system. The 'R' value—the minimum applied stress divided by the maximum applied stress—was constant at R = 0.1. Testing was conducted at 15 Hz for all tests presented. The runout point was fixed at 5 million (5×10^{6}) cycles. Of the reported fatigue testing data, each data point on an S—N curve figure is the median value calculated from three test specimens accompanied by the calculated standard error of the three test specimens.

2.5. Metallography

Specimens were hot mounted in resin before being progressively ground to a finer finish from P320 to P2500 grit. Samples were then polished with a solution of 90 mL fumed silica and 10 mL of 30 % concentration hydrogen peroxide. Finally, the polished samples were etched in accordance to ASTM E407 with Kroll's reagent (6 % nitric acid, 2 % hydrofluoric acid, 92 % water) for approximately 10 s to reveal microstructural features.

Micrographs were captured using a secondary electron (SE2) detector on a Zeiss ULTRA scanning electron microscope in the Advanced Microscopy Laboratory (Dublin, Ireland) and using a Zeiss Axiovert optical microscope. For quantification of microstructural features, segmentation of grains was first performed in Photoshop before conducting feature measurements in MIPAR software. In testing quantified microstructural features for statisti-

cal significance between the sample mean values, tests were conducted at a 95 % confidence interval with Bonferroni correction applied when the means of multiple samples were compared simultaneously.

2.6. X-ray diffraction

Samples were ground and polished – as described in the *Metallography* subsection – before being scanned on a Bruker D8 Advance diffractometer over 33–90°2θ at a step size of 0.02° and dwell time of 2 s per step. A corundum standard reference material 1976b sample was scanned and the resultant peak full-width at half maximum (FWHM) values were measured using Origin Pro 9.0 software from OriginLab (Massachusetts, USA). This enabled the determination of the inherent instrument peak broadening which was to be accounted for when FWHM values for the heat treated samples were measured. The β-phase volume fraction and lattice parameters of each heat treated sample were calculated from the collected X-ray diffraction patterns using the Reitveld refinement method [29] in MAUD software (version 2.94) [30].

3. Results

3.1. Static characterisation of bimodal Ti-6Al-4V microstructures

3.1.1. Variation of T_{max}

The first experiments focused on the outcome of altering the maximum cycle temperature, T_{max}, with the view to better understand the role of the T_{max} parameter in determining the microstructure formation and corresponding tensile test properties of a cyclically heat-treated part. A range of T_{max}—below, on the cusp of, and beyond the β-transus—were chosen to be studied, as shown in Table 2. As a point of reference, a more conventional heat treatment was also included: 950 °C for 2 h, followed by an air cool.

Kaushik et al. [31] recently utilised differential scanning calorimetry to experimentally pinpoint the β-transus temperature to approximately 993 °C ± 2 °C for printed grade 23 titanium. Zhang et al. [32] employed the same technique and measured the β-transus to be within 986 °C for this material. It is therefore anticipated that the β-transus temperature for the material used in this study to be in the neighbourhood of 990 °C. The treatments conducted at $T_{max} = 1000$ °C and $T_{max} = 1050$ °C are therefore supertransus heat treatments.

Table 2
Parameters of the static (bottom row) and cyclical profile heat treatments (preceding rows) employed in this section. All cyclical treatment parameters except the cycle maximum temperature, T_{max}, are fixed.

Initial heating rate, from atmospheric conditions to T_{max} (°C/min)	Minimum cycling temperature, T_{min} (°C)	Maximum cycling temperature, T_{max} (°C)	Cycling period heating & cooling rate (°C/min)	Number of cycles experienced	Cooling regime
5	850	900 950 980 1000 1050	2	3	Air cool (10 °C/s[1])
5	n/a	Statically held at 950 °C	n/a		2 h soak

Fig. 2 illustrates the different microstructures which resulted from varying solely the maximum cycle temperature, T_{max}. Fig. 2 (a)–(c) shows lamellar microstructures of increasing coarseness as the value for T_{max} rises and approaches the β-transus temperature. Fig. 2 (d) and (e) reveals that a bimodal microstructure was rendered through treatment at a T_{max} value of 1000 °C and 1050 °C, respectively, which consist of large primary α grains surrounded by a lamellar matrix. It is seen in Fig. 2 (e) that treatment at a T_{max} value of 1050 °C—beyond the β-transus temperature— yields the coarsest microstructural features of the sample set with larger primary α grains compared to Fig. 2 (d). Fig. 2 (f) presents the result of a more conventional heat treatment at 950 °C for 2 h. This microstructure bore fine, acicular grains most similar to Fig. 2 (a). Although the sample in Fig. 2 (a) experienced a lower maximum temperature than the sample in Fig. 2 (f), the cyclical treatment profile evidently enabled grain growth and globularisation to a larger degree than the more conventional treatment profile.

Examining the tensile test performance of the cyclically-treated samples, as seen in Fig. 3, the UTS and yield strength values are quite consistent. Though there are substantial changes to the α-phase morphology evident in the micrographs of Fig. 2, UTS and yield strength values hover around 1000 MPa and 900 MPa, respectively. Considering the ductility of the test samples, the sub-transus T_{max} samples (900 °C; 950 °C; 980 °C) exhibited effectively similar engineering strains of approximately 13.5 %. One of the samples rendered with a bimodal microstructure (T_{max} = 1000 °C) showed an elevated ductility, to within 15 %, while the other bimodal microstructure sample (T_{max} = 1050 °C) showed a sharp reduction in ductility, to approximately 10 %. The reference heat treatment sample (950 °C for 2 h) showcased the best tensile strength performance of the sample group with mean UTS and yield values of approximately 1200 MPa and 1100 MPa, respectively. This significant gain over the cyclically-treated samples might be attributed to fine, acicular grain morphology presented in Fig. 2 (f).

A bimodal microstructure, consisting of large primary α-phase grains within a fine-grained matrix, was rendered in parts when treating to a maximum cycle temperature, T_{max}, of 1000 °C or above as seen in Fig. 2. From Fig. 3, the sample treated at T_{max} = 1000 °C exhibited the best tensile performance of the cyclically-treated samples, with UTS values within 1000 MPa and fracture strains of approximately 15 %. Although the sample treated at T_{max} = 1050 °C also possessed a bimodal microstructure, it displayed a sharp drop in ductility, down to within 10 %.

Fig. 4 plots the percentage volume fraction of retained β-phase in each sample. Phase volume fraction calculations were achieved through the application of the Rietveld method to XRD data. The results show that there is a minor increase in the percentage of retained β-phase as T_{max} rises from 900 °C through to the cusp of the β-transus at 1000 °C but a major increase in retained β-phase at a T_{max} value of 1050 °C. The conventionally-treated sample was rendered with a similar level of retained β-phase to the cyclically-treated samples—so neither treatment approach was no more beneficial than the other in this regard.

Saunders et al. [33] modelled and also experimentally measured the volume fraction of β-phase at temperatures approaching the β-transus for grade 5 titanium. They found the volume fraction of β-phase to rise from approximately 45 % up to 100 % as the target temperature increased from 900 °C to 1000 °C. However, air
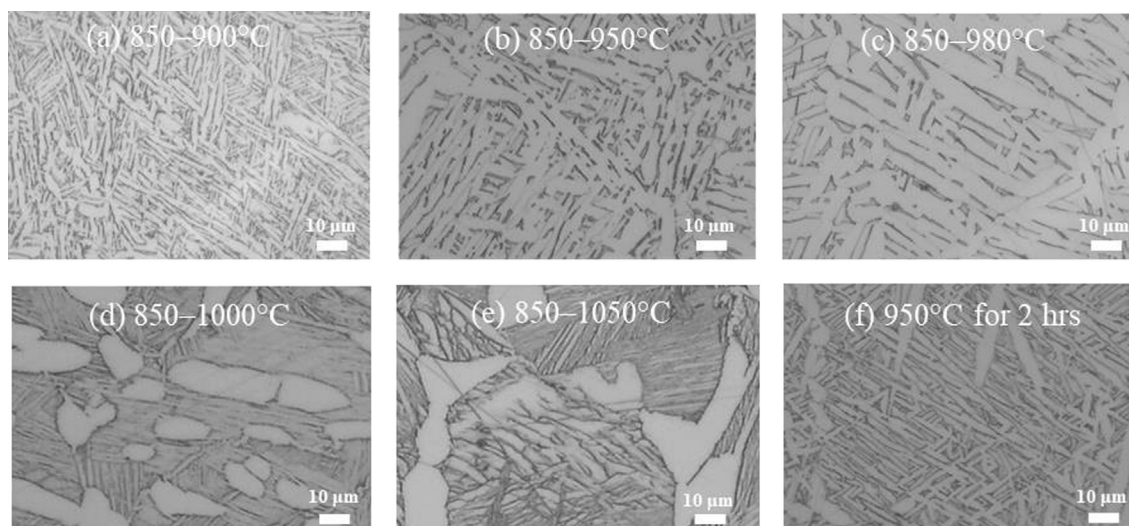

Fig. 2. Optical micrographs of cyclically treated samples with different maximum cycle temperatures, T_{max}: (a) 900 °C; (b) 950 °C; (c) 980 °C; (d) 1000 °C; (e) 1050 °C; (f) a more conventional heat treatment at 950 °C for 2 h followed by an air cool. All micrographs were captured at the same magnification.
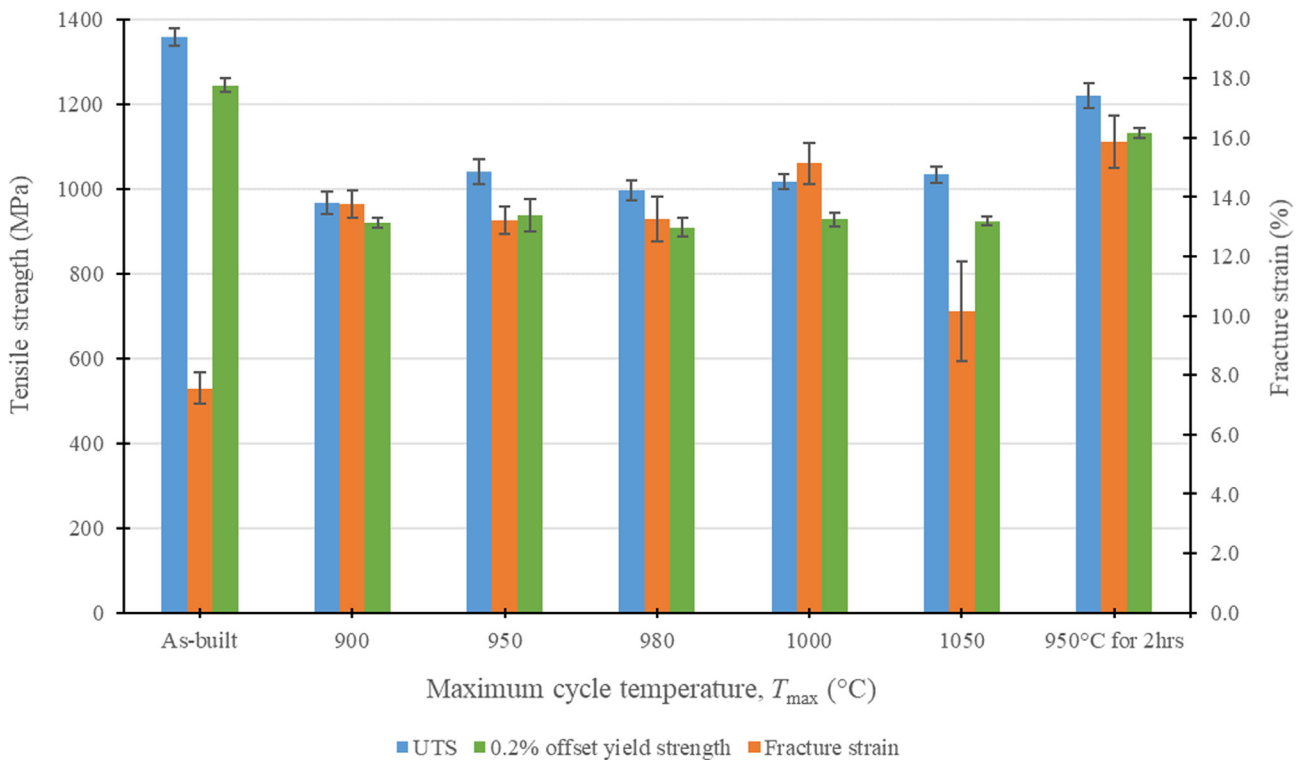
Fig. 3. Mean UTS, yield and fracture strain values for different T_{max} set points. Tensile performance for the as-built and reference heat treatment samples bookend the graph.
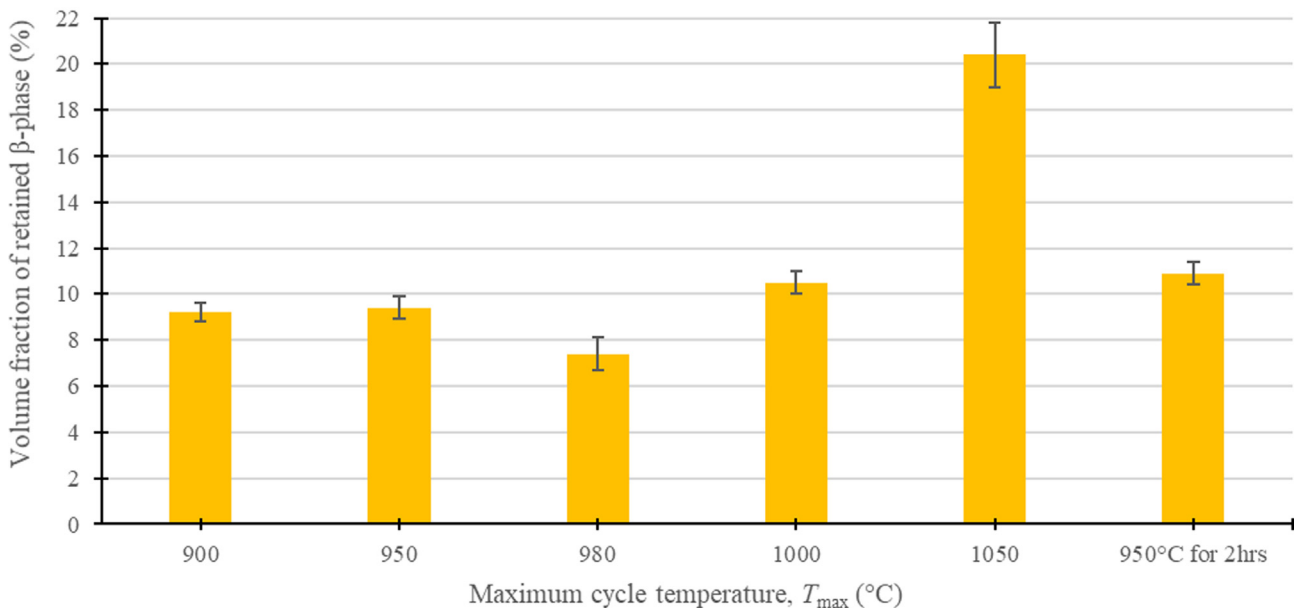

Fig. 4. Percentage of retained β-phase plotted for different T_{max} values as well as the reference heat treatment (950 °C for 2 h).

cooling treated parts across this temperature range yielded comparable volume fractions of β-phase. The cooling rate was sufficiently low enough to enable equilibrium transformation of the β-phase while also retaining a higher volume fraction of β-phase than what might be achieved by employing a slow, furnace cool.

Cooling from a T_{max} value of 1050 °C—comfortably above the β-transus temperature − retained 20 % volume fraction of β-phase. Fig. 2 (e) shows the severe grain coarsening which accompanied treatment at this temperature. Theoretically, a greater volume fraction of the more ductile β-phase should translate into the best
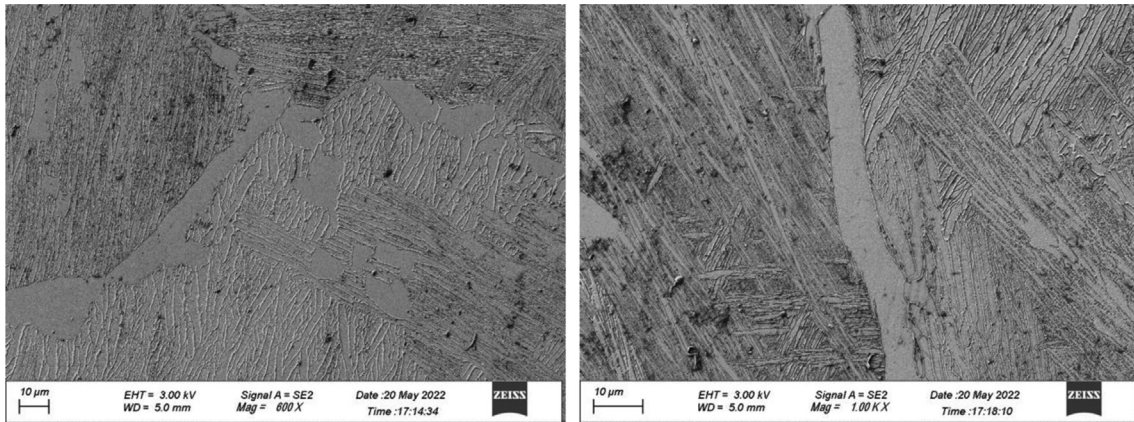
Fig. 5. Grain boundary α-phase present in the sample treated at T_{max} = 1050 °C.

fracture strain performance for this sample. Closer examination of the 1050 °C sample microstructure, presented in Fig. 5, revealed persistent α-phase at prior β-phase grain boundaries. Liu et al. [34] recently showed the detrimental impact of grain boundary α-phase on tensile ductility which serves to explain the impaired ductility of this bimodal microstructure.

3.1.2. Variation of T_{min}

Once it was established that it was necessary for T_{max} to be set at the cusp of the β-transus temperature to render parts with a bimodal microstructure, the next experiments focused on understanding the role of the minimum cycle temperature, T_{min}, and how this variable affects the microstructure formation and tensile performance. Table 3 presents the three cycle minimum temperatures chosen: 800 °C; 850 °C; 900 °C.

Saunders et al. [33] reported that the volume fraction of α-phase climbs from 55 % up to 85 % as the material temperature drops from 900 °C to 800 °C. Values in this range were chosen for the minimum cycling temperature in an attempt to promote variation in the resulting microstructures and the corresponding tensile test properties.

Fig. 6 displays the microstructural formation resulting from each of the three T_{min} values, respectively. There are no apparent differences between the three microstructures, all of the samples share the common features of large, often globular α-phase grains within a fine dual-phase matrix.

Tensile test performance for the samples is displayed in Fig. 7. The results are comparable, with UTS, yield and fracture strain values falling within the standard error range of each other. Altering the minimum cycle temperature does not invoke a discernible change in either the microstructure or tensile test performance of the material.

The micrographs of Fig. 6 and the tensile test performance in Fig. 7 offers evidence for the negligible impact that T_{min} value variation wields over microstructure formation and mechanical properties. Fig. 8 presents the changes in grain diameter (α-phase lath thickness) across the range examined. The fine α-phase grains underwent a statistically significant reduction from approximately 0.53 μm to 0.43 μm as T_{min} rose from 800 °C to 900 °C. There was no significant thickening of the large grains across the sample temperature range. Fig. 9 illustrates the growth of the large, primary α-phase grains paired with a minor reduction in the area of fine α-
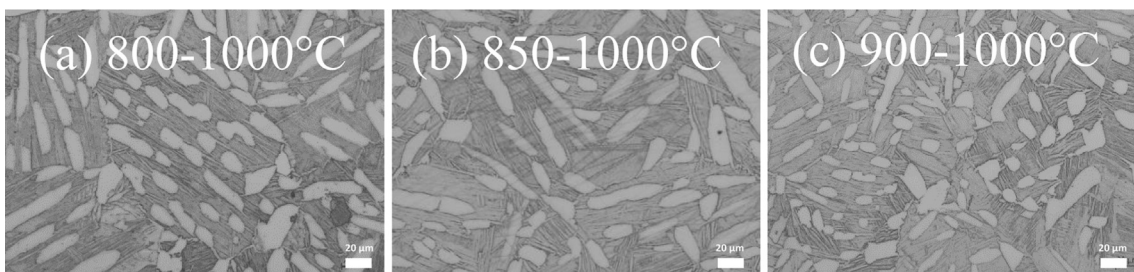
Table 3
Parameters of cyclical profile heat treatments employed in this section. All parameters except the cycle minimum temperature, T_{min}, are fixed.

Initial heating rate, from atmospheric conditions to T_{max} (°C/min)	Minimum cycling temperature, T_{min} (°C)	Maximum cycling temperature, T_{max} (°C)	Cycling period heating & cooling rate (°C/min)	Number of cycles experienced	Cooling regime
5	800 850 900	1000	2	3	Air cool (10 °C/s[1])

Fig. 6. Microstructures of samples with different minimum cycle temperatures, T_{min}: (a) 800 °C; (b) 850 °C; (c) 900 °C. All other heat treatment profile parameters remained constant across the samples. The micrographs were captured at the same magnification.

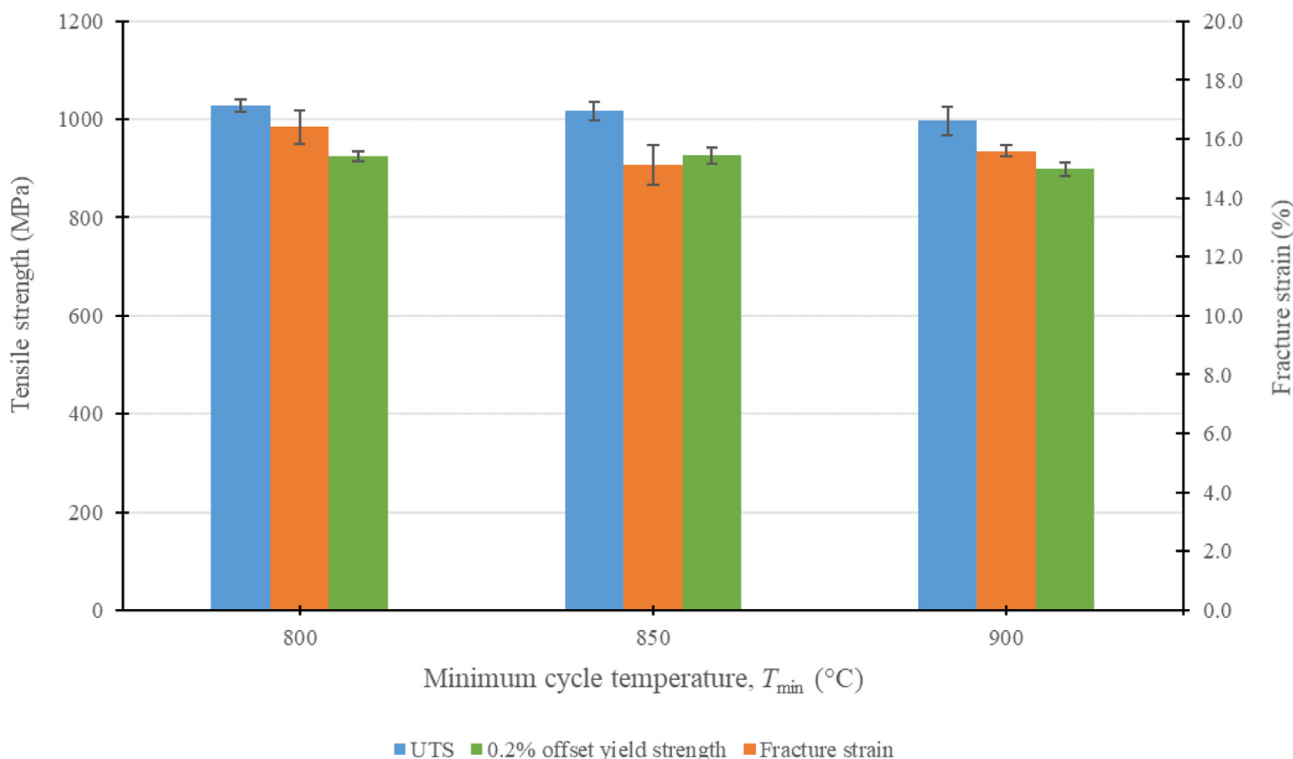## Tensile performance vs. minimum cycle temperature

Fig. 7. Tensile test performance for cyclically treated samples with different minimum cycle temperatures, T_{min}.

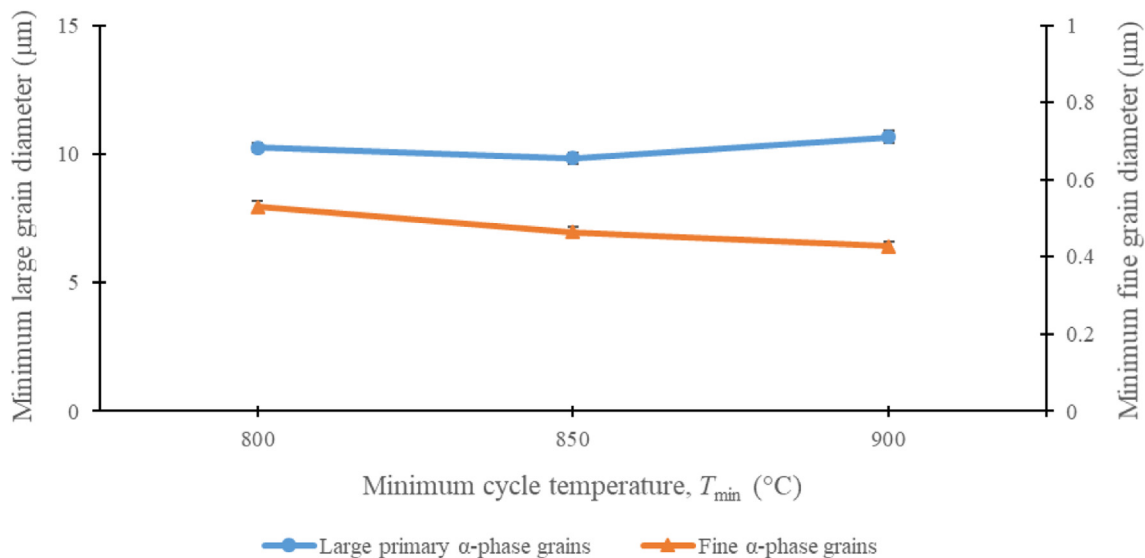## Grain diameter vs. minimum cycle temperature

Fig. 8. Evolution in bimodal grain diameters (thicknesses) as the minimum cycle temperature, T_{min}, value changes.

phase grains as the T_{min} value increases. Nevertheless, it is clear that both the material tensile strength and ductility are not sensitive to minor changes in bimodal microstructure morphology.

3.2. Number of cycles experienced

After determining a critical T_{max} value, and the insignificance of the T_{min} value, the last cyclical treatment parameter to be assessed

was the number of cycles experienced, i.e. the effective soak time. Table 4 outlines the sample treatment strategies chosen. Critically, samples were exposed to either 1, 3, 6 or 9 thermal cycles which varied the effective soak time from 2.5 h (1 cycle) to 22.5 h (9 cycles).

Optical micrographs for the samples are depicted in Fig. 10. A bimodal microstructure of large, primary α-grains (light grey) within a fine-grained, dual phase matrix (dark grey) is evident
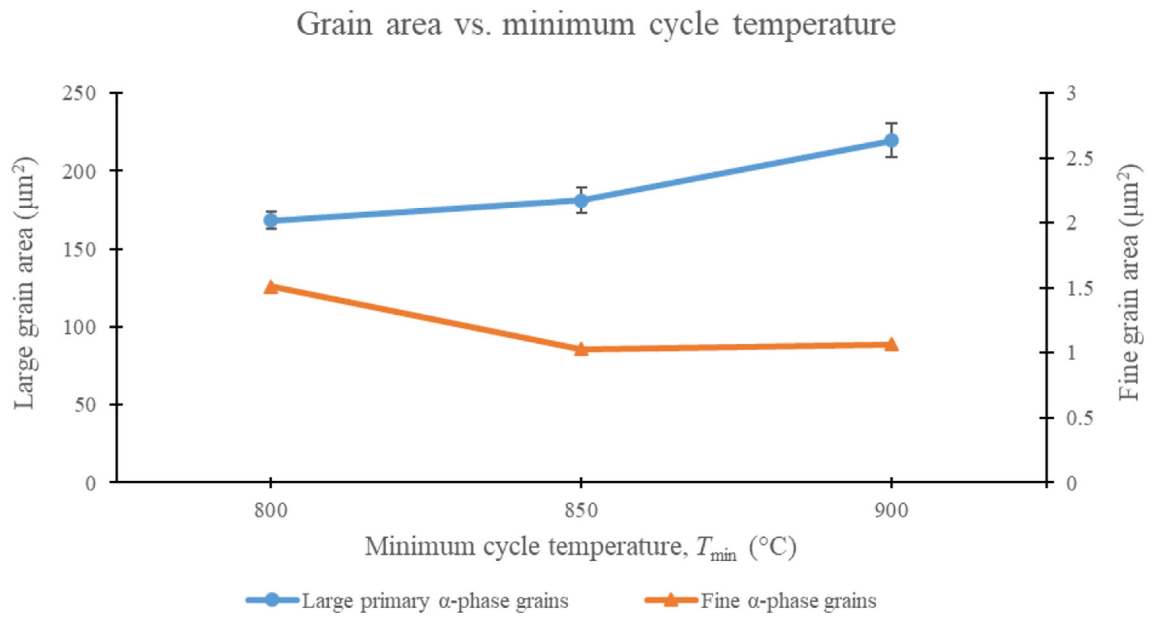
Fig. 9. Evolution in bimodal grain area as the minimum cycle temperature, T_{min}, value changes.

Table 4
Parameters of cyclical profile heat treatments employed in this section. All parameters except for the number of thermal cycles each sample experienced are fixed.

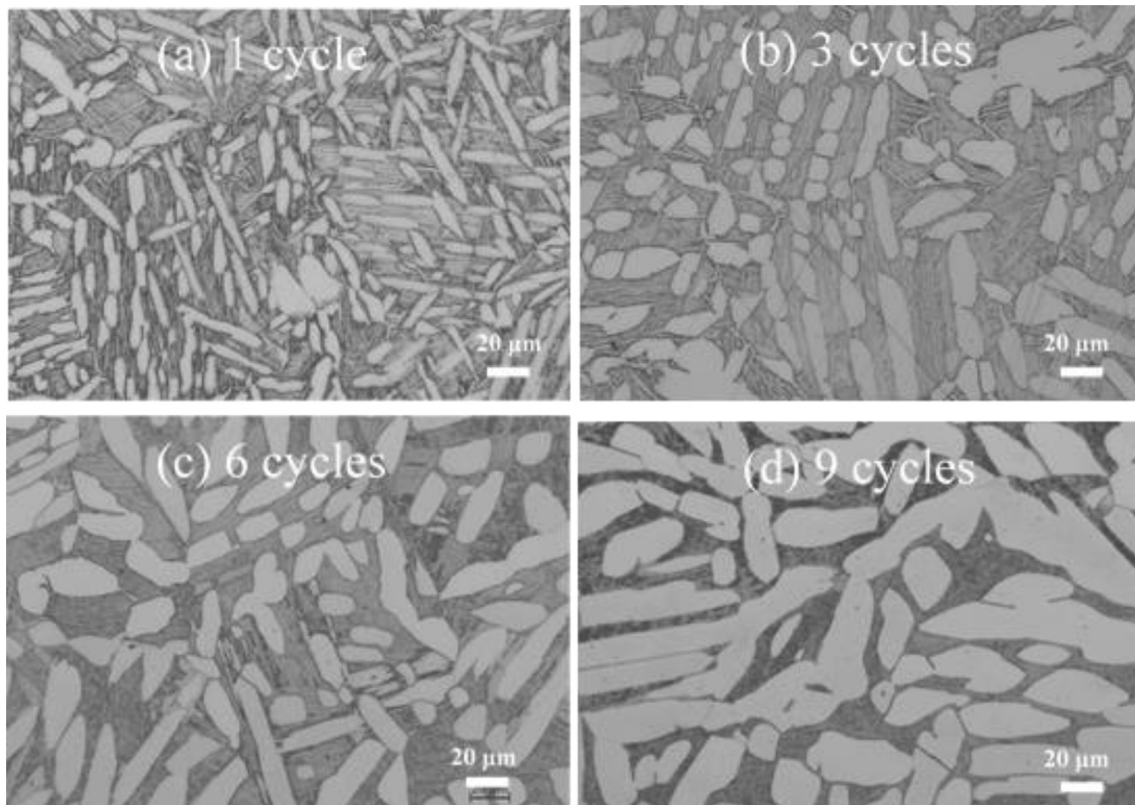| Initial heating rate, from atmospheric conditions to T_{max} (℃/min)	Minimum cycling temperature, T_{min} (℃)	Maximum cycling temperature, T_{max} (℃)	Cycling period heating & cooling rate (℃/min)	Number of cycles experienced	Cooling regime
5	850	1000	2	1 3 6 9	Air cool (10 ℃/s^1)

Fig. 10. Optical micrographs of samples subjected to different numbers of thermal cycles in a cyclical-profile heat treatment: (a) 1 cycle, (b) 3 cycles, (c) 6 cycles, (d) 9 cycles. All micrographs were captured at the same magnification.

for each sample. There is a clear coarsening of the primary α-phase grains as the number of experienced cycles rises. Fig. 11 offers a closer view of the fine-grained, dual phase matrix for the '9 cycles' sample.

The tensile performance of the samples are depicted in Fig. 12. The UTS and yield strength values are consistently within 1000 MPa and 900 MPa, respectively. Ductility values display more scatter with a range of 14–16 %. The number of cycles experienced
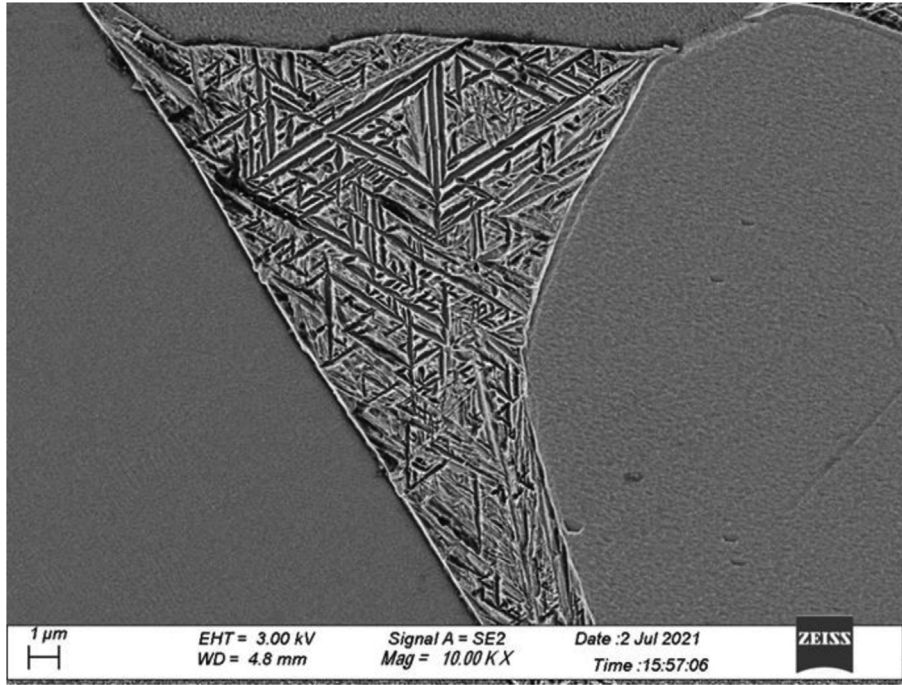

Fig. 11. SEM detail on fine-grained, dual phase region surrounded by large, primary α-phase (lighter grey) for the '9 cycles' sample.
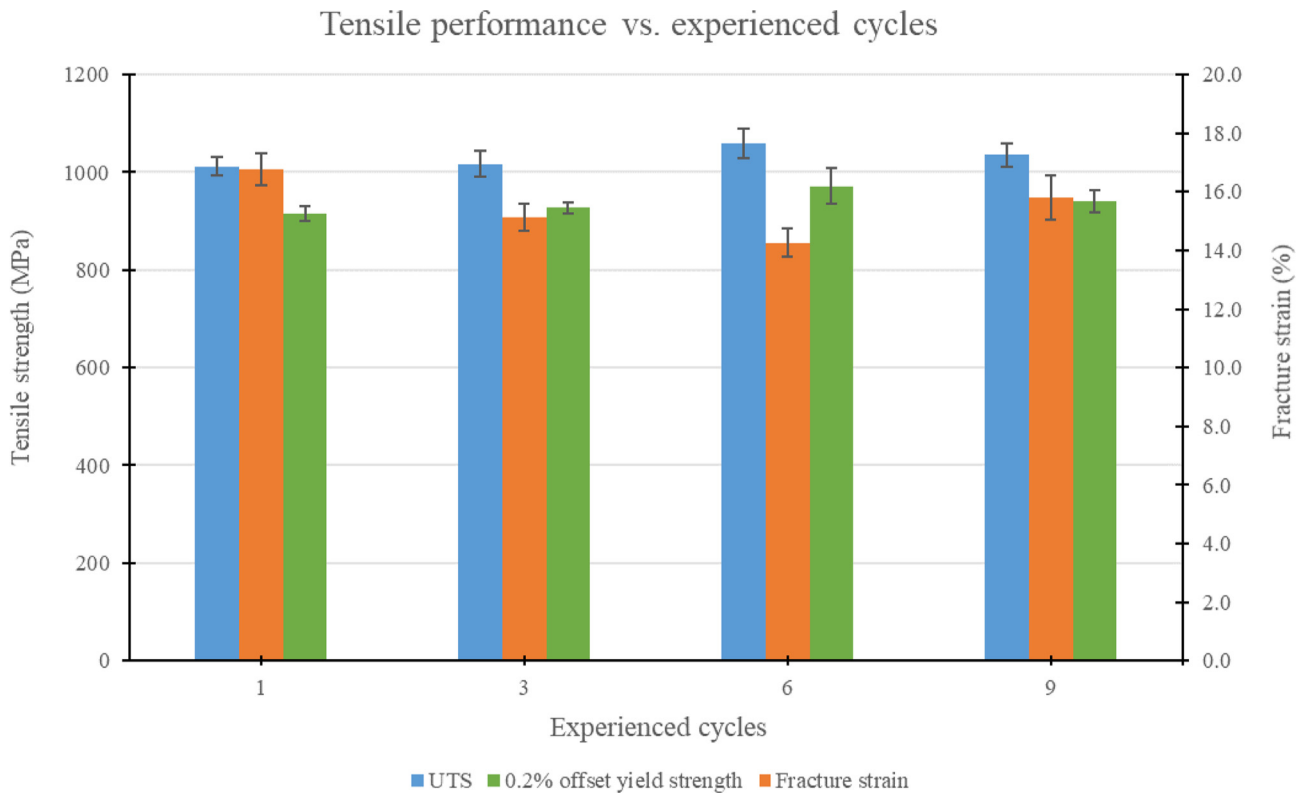

Fig. 12. Tensile test performance of samples which experienced different numbers of thermal cycles, varying the effective soak time for each sample.
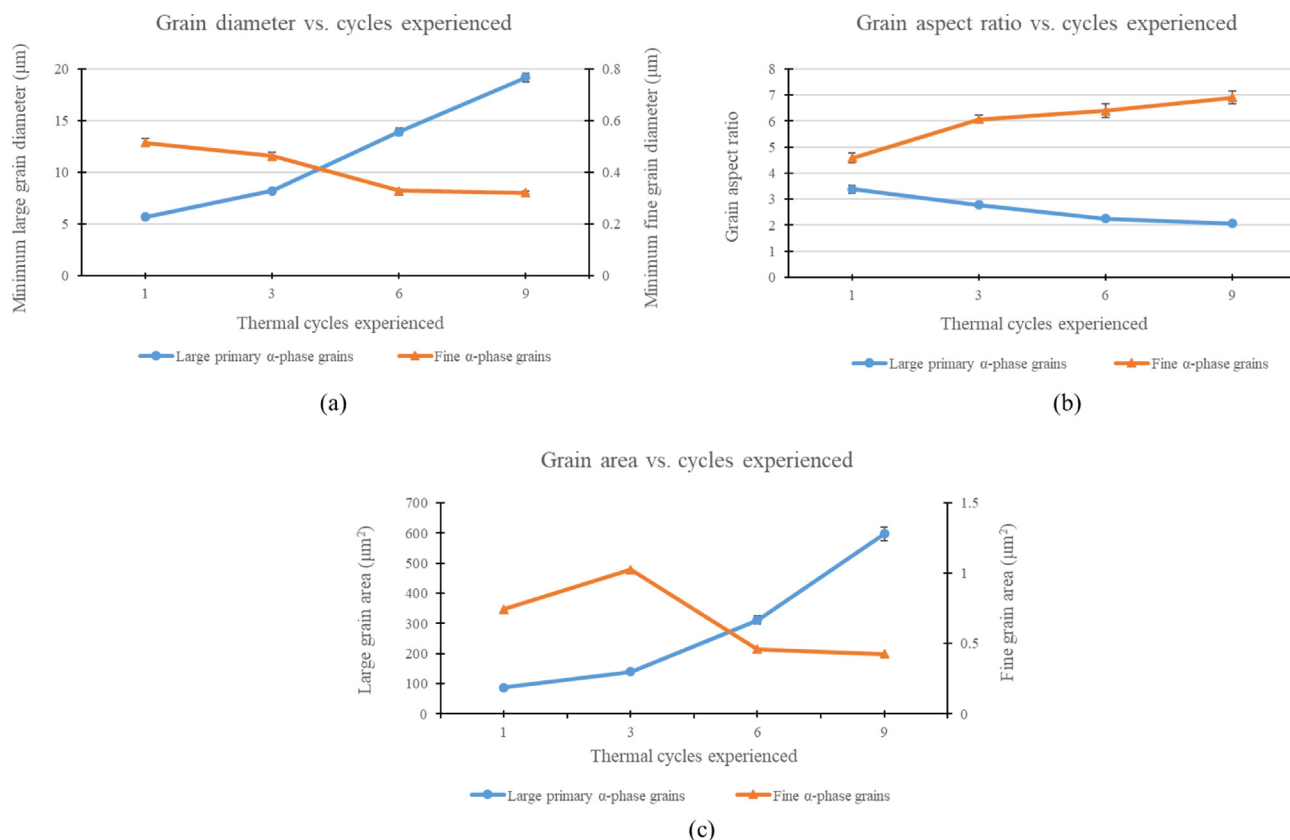
(a)

(b)

(c)

Fig. 13. Changes in bimodal (fine and large) grain morphology as the number of heat treatment cycles experienced increases: (a) grain diameter, (b) grain aspect ratio, (c) grain area.

by a sample appears to have no bearing on the tensile test performance. Volume percentage of retained β-phase, calculated from XRD data, for the samples returned values of within 10 % retained β-phase so the number of thermal cycles is having no impact upon this phase volume ratio. Increasing the number of cycles experienced effectively raises the soak time that the material is treated between the temperature limits, T_{max} and T_{min}. In this instance, the effective soak time ranges 2.5–22.5 h.

As seen in the optical micrographs of Fig. 12, the number of cycles experienced by the material has a profound impact upon microstructure morphology. Fig. 13 charts the evolutions in both fine and large α-phase grain morphologies as the number of treatment cycles rises. However, the microstructural features evolution is not translating in to discernible variation in the tensile test performance, presented in Fig. 12.

The micrographs in Fig. 10 show the dramatic coarsening of the primary α-phase as the number of experienced cycles rises. Increasing the number of cycles experienced effectively raises the soak time that the material is treated between the temperature limits, T_{max} and T_{min}. In this instance, the effective soak time ranges 2.5–22.5 h. Fig. 13 charts the evolutions in both fine and large α-phase grain morphologies as the number of treatment cycles rises. Considering the large, primary α-phase grains in Fig. 13 (a), there is significant coarsening of the average grain diameters from within 5 μm to 18 μm. In Fig. 13 (b) the average aspect ratio of the large grains reduces significantly from approximately 3 to 2. In Fig. 13 (c) there is clear swelling of the large, primary α-phase grains. The primary grains grow by approximately 600 % in area across the sample range. The primary α-phase grains are getting bigger and rounder as the number of cycles increases. Conversely, the α-phase grains within the fine-grained matrix of these microstruc-

tures are significantly thinning, reducing in area as the mean grain aspect ratios are climbing, which might be seen in Fig. 13 (a), (b) and (c). Raising the number of thermal cycles experienced by the material is serving to further polarise the microstructure—with ever larger primary α-phase grains and ever finer matrix α-phase grains.

3.3. Altering the cooling regime

Fig. 14 reports the effect of altering the cooling rate of cyclically treated samples upon tensile test performance. The parts experienced 1 thermal cycle from 850 °C to 1000 °C. The water-quenched sample is considerably stronger but also considerably less ductile than the air-cooled sample. The micrographs in Fig. 15 showcase the stark difference in microstructure morphology between the samples.

It is apparent from the micrographs in Fig. 15 that fresh martensite has been generated in the water-quenched sample which experienced a cooling rate of approximately 120 °C/s[1] as it was cooled from a T_{max} value of 1000 °C. It is estimated that the applied cooling rate must exceed 16 °C/s[1] [35,36] to induce martensitic transformation (β → α') from this temperature. The fine-grained, high aspect ratio grains visible in Fig. 15 are the hallmarks of a martensitic Ti-6Al-4V microstructure. This offers clear confirmation that the water quenching of heat treated Ti-6Al-4V parts will undoubtedly induce the formation of non-equilibrium phases which are detrimental to mechanical properties, evinced in increased strength and reduced ductility observable in Fig. 14. The rate at which parts are cooled from the T_{max} temperature has a profound influence on the rendered microstructure and mechanical properties.

3.4. Dynamic characterisation of bimodal Ti-6Al-4V microstructures

3.4.1. Fatigue performance of cyclically-treated Ti-6Al-4V samples

Fig. 16 and Fig. 17 present the S–N or Wöhler curves for printed Ti-6Al-4V material in the as-built, cyclically-heat-treated and annealed conditions. The cyclically heat treated samples, '1 cycle' an '9 cycles' were subjected to almost the same treatment profile: T_{min} and T_{max} were set to 850 °C and 1000 °C respectively for both samples. While the 9 cycles samples experienced 9 thermal cycles, the 1 cycle sample only experienced a single thermal cycle.

The as-printed sample performed strongly but did not exhibit a fatigue strength at the maximum stresses tested, as seen in Fig. 16. The '1 cycle' sample experienced the cyclical heat treatment parameters listed in the first row of Table 4. This sample demonstrated a clear fatigue strength of 500 MPa at the set runout point of 5 million cycles, visible in Fig. 17. However, this cyclically-treated sample performed worse than the as-printed material in the low-cycle regime, at maximum applied stresses of 600 MPa and greater. The '9 cycles' sample displayed a fatigue strength of

400 MPa—100 MPa lower than that measured of the 1 cycle sample. Finally, printed Ti-6Al-4V parts were also subjected to a more conventional, single stage heat treatment: 950 °C for a 2-hour soak followed by air cooling. This sample exhibited the highest fatigue strength of the group at 600 MPa.

The strong performance of the as-printed material in the low-cycle region of Fig. 16 can be attributed to the very fine grain structure, with α'-phase grain thicknesses in the order of 0.23 μm ± 0. 01 μm. Fine-grained microstructures reduce effective dislocation slip lengths and pave tortuous crack trajectories which hinder crack growth and raise fatigue strength [37]. In their recent study on the low-cycle fatigue performance of SLM'd Ti-6Al-4V, Xi et al. [38] showed evidence relating how higher tensile yield strength can translate to better fatigue performance in the low cycle region. This further supports why as-built specimens displayed elevated low cycle performance.

The strength afforded by these fine grains was undermined in the high-cycle region as the as-built sample did not exhibit a definite endurance limit. Although two of the specimens tested at a max. stress of 500 MPa reached runout at 5 million cycles without failing, the third specimen failed at approximately 1.76 million cycles. The broad scatter in measured values, evident in the standard error bars, is particularly pronounced in the as-built sample data points of Fig. 16. The fatigue performances of all of the samples in this study were comparable to published works which tested effectively defect-free printed parts and reported fatigue strengths ranging 410–550 MPa [39–41]. Surface tensile residual stress in as-printed Ti-6Al-4V material can facilitating surface crack initiation in fatigue specimens [42], while subsurface residual stress can be as high as the yield stress of the material [43]. Residual stress is therefore likely responsible for the increased scatter and indeterminate fatigue strength of the as-built sample.

Fig. 17 displays the S–N plots for the heat-treated samples. Comparing the cyclical profile treatments, the 1 cycle sample and 9 cycles samples exhibited fatigue limits of 500 MPa and 400 MPa, respectively. Though the disparity in microstructural features between the 1 cycle and 9 cycles samples is apparent in Fig. 10, these differences did not translate to changes in the tensile performance (Fig. 12). Microstructural differences between the samples amounted to varying size, shape and volume fraction of the primary α-phase grains. The 9 cycles sample primary α-phase grains were 600 % larger—Fig. 13 (c)—and almost 4 times as thick—Fig. 13 (a)—as equivalent grains in the 1 cycle sample. Although the 9 cycles sample possessed a finer dual-phase grain matrix structure, the larger primary α-phase grains were ultimately detrimental to the fatigue performance of the material.
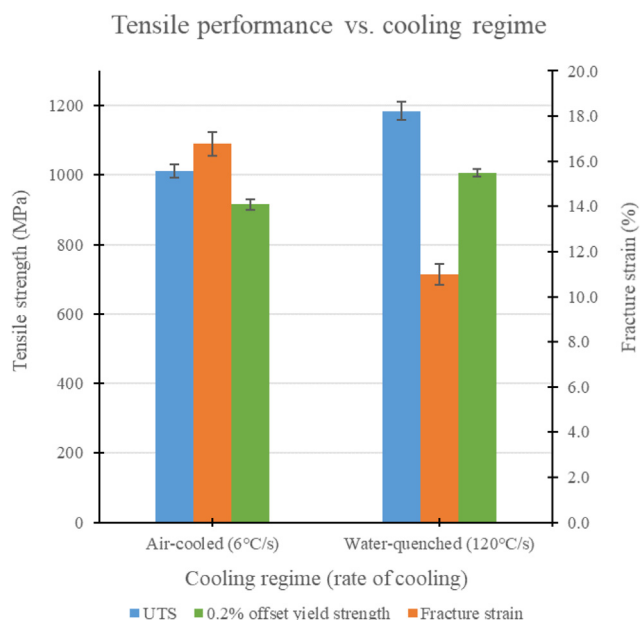

Fig. 14. Tensile performance of samples which received the same cyclical heat treatment but different cooling regimes.
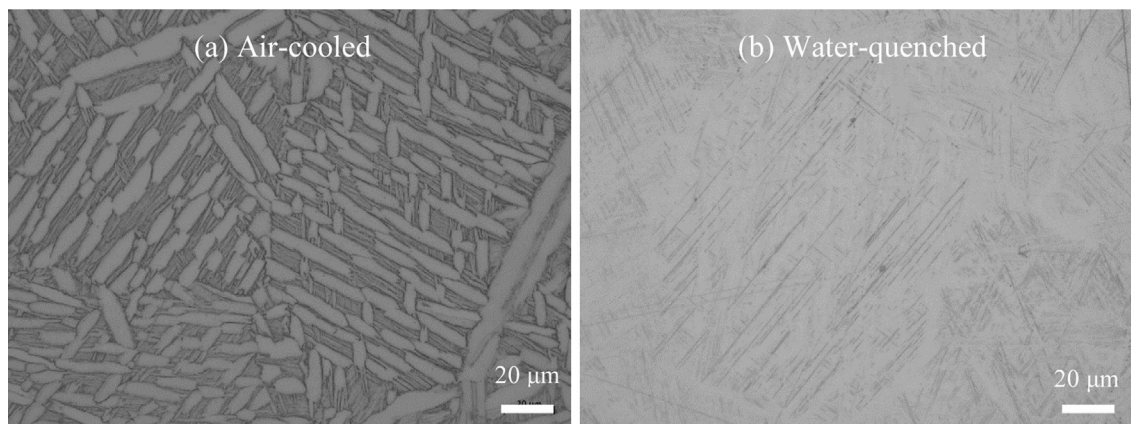

Fig. 15. Optical micrographs of cyclically-treated samples which experienced: (a) air cooling, and (b) water quenching. Captured at 50x magnification.
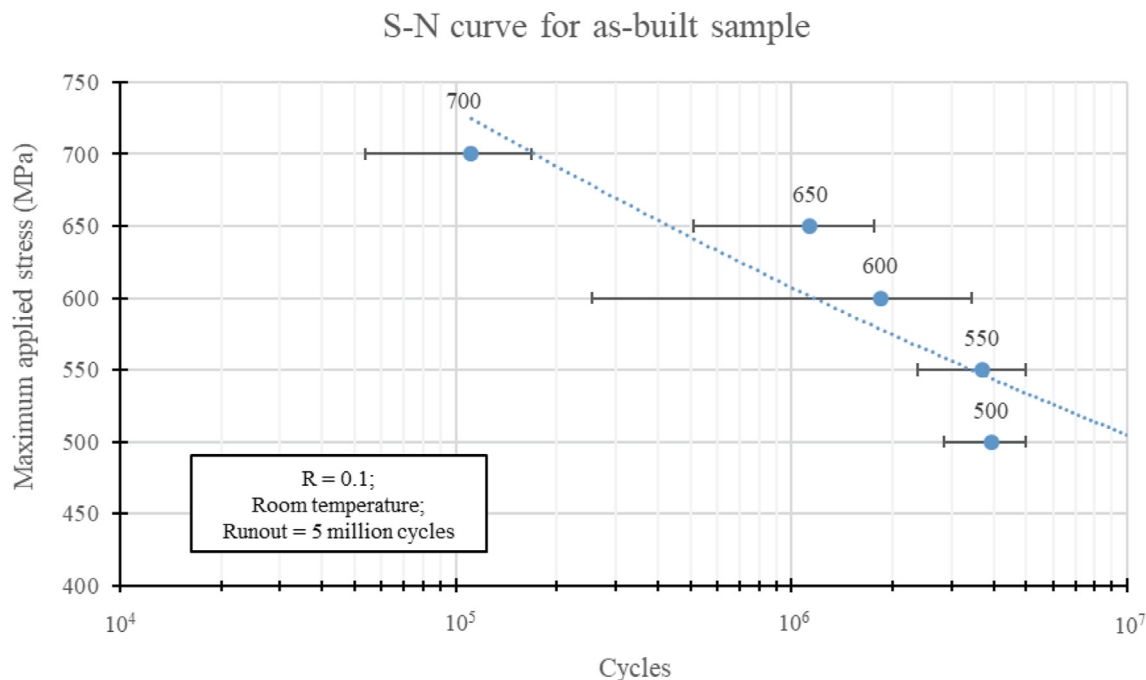
Fig. 16. High cycle fatigue performance of as-printed and machined Ti-6Al-4V material.
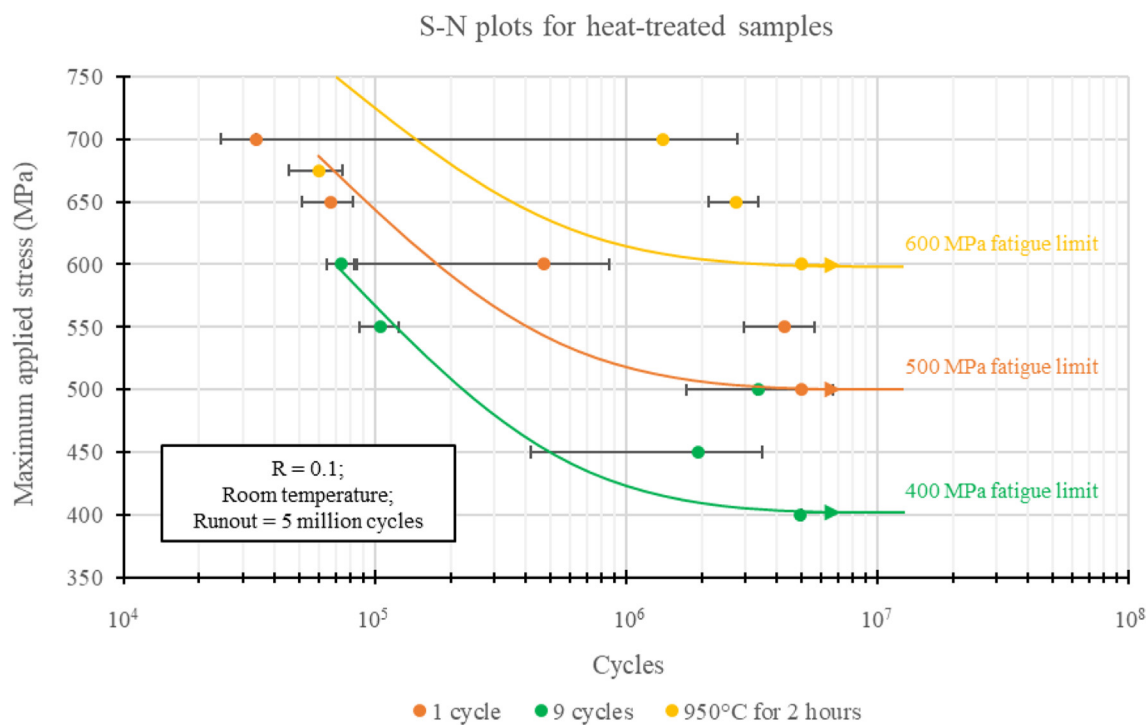

Fig. 17. High cycle fatigue performance of printed and heat-treated Ti-6Al-4V material. The determined fatigue limit for each sample as well as a loose curve fit is included.

Wu et al. [25] compiled and analysed 75 sets of fatigue data for Ti-6Al-4V material with different microstructures (bimodal, lamellar and equiaxed). Concerning bimodal microstructures, they reported a correlation relating rising fatigue strength with finer primary α-phase grain size. The deviation in performance between the cyclically-treated samples can therefore be attributed to the size and shape of the primary α-phase grains. The authors also reported evidence showing how there is a 'sweet spot' for volume fraction of primary α-phase, in the region of 30–50 %. Outside of

this region—for volume fractions of either less than 30 % or greater than 50 %—there was evidence showing a significant drop in HCF strength. The 9 cycles sample in this study contained approximately 37 % primary α-phase while the 1 cycle sample constituted 49 %. Both of the samples tested were within the bounds of this so-called 'sweet spot' and yet the respective fatigue strengths are significantly different.

The single stage heat treatment sample (950 °C for 2-hours) exhibited the highest fatigue strength of the group at 600 MPa,
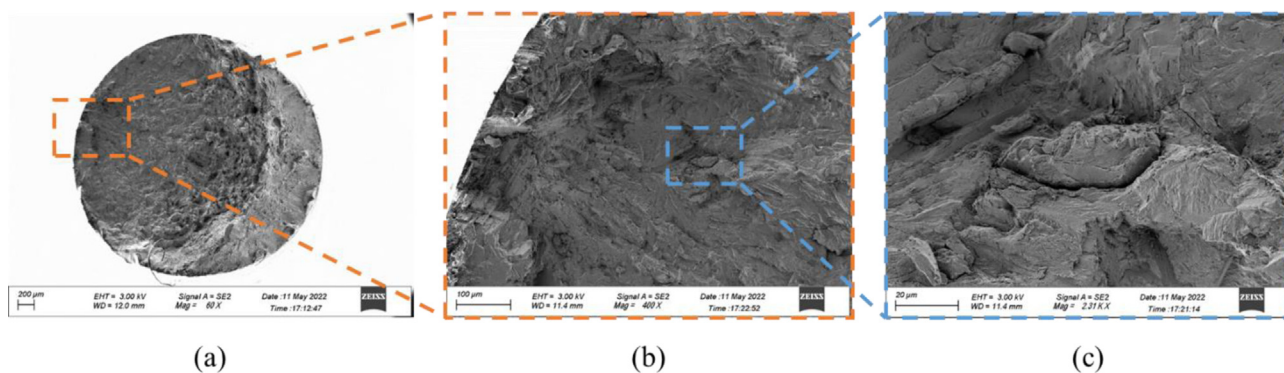
Fig. 18. Fractograph of a '1 cycle' sample specimen tested at 600 MPa. Number of cycles achieved: 82,367 cycles.
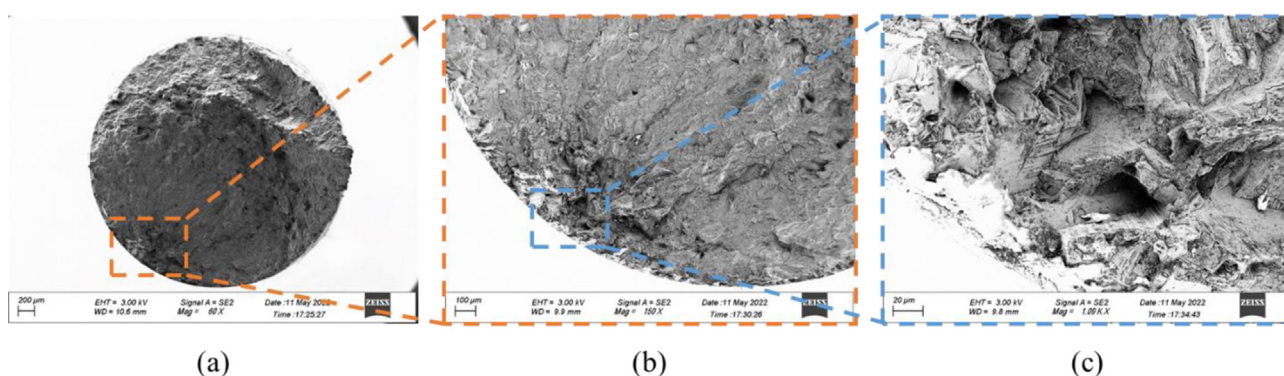

Fig. 19. Fractograph of a '1 cycle' sample specimen tested at 600 MPa. Number of cycles achieved: 1,251,750 cycles.

100 MPa stronger than the 1 cycle sample. Li et al. [44] compared the HCF performance (at R = 0.1; 10 Hz; room temperature) of lamellar and bimodal Ti–6Al–2Zr–1Mo–1 V microstructures with two notch concentration factors (K_t = 1, 3). They reported that the lamellar microstructure to out-perform the bimodal counterpart at both notch concentration factors. The authors reasoned that the element partitioning effect in the lamellar matrix component of the bimodal microstructure was responsible for the impaired fatigue strength. The element partitioning effect could here too offer an explanation as to why the HCF performance differs so greatly between the bimodal and lamellar microstructure samples. Tan et al. [45] recently published evidence showing that cracks initiate at the primary α-phase grain interfaces in bimodal titanium microstructures. Zuo et al. [24] found internal fatigue cracks to initiate at the boundary of or within primary α-phase grains in bimodal microstructures. The large primary α-phase grains could also have served as potent crack initiation to further hinder HCF performance in the bimodal microstructures.

In their survey of HCF performance of additively manufactured Ti-6Al-4V, Rao et al. [46] reported the within sample variation to be generally very large, in the order of two degrees of magnitude [46]. This corroborates the current work in which all of the samples demonstrated broadly scattered performance, particularly the as-built and 9 cycles samples. Fig. 18 and Fig. 19 presents fatigue fractographs for two '1 cycle' specimens tested at 600 MPa. The specimen in Fig. 18 only achieved approximately 82,000 cycles until failure and Fig. 18 (b) offers a detailed view of the likely crack initiation site, with Fig. 18 (c) presenting a closer image of a crack. For the fracture surface shown in Fig. 19, this specimen achieved within 1.25 million cycles before failure. In both sets of frac-

tographs, failure cracks were either surface of sub-surface in origin. Günther et al. [37] reported all of their SLM'd and annealed Ti-6Al-4V HCF specimens failed due to surface defects (surface crack initiation). The scatter in fatigue data in this study might be attributed to the surface conditions of the machined specimens.

4. Conclusions

In the present research, the effect of cyclical heat treatment parameters (maximum temperature, minimum temperature, number of cycles and cooling rate) on the grain morphology, phase composition and mechanical performance (static and dynamic) has been evaluated and compared to a typical lamellar microstructure.

The temperature from which a treated Ti-6Al-4V part is cooled and the cooling rate will determine whether or not a bimodal microstructure will form. In this instance, samples needed to be treated at the cusp of the β-transus temperature (1000 °C) and air cooled to form a bimodal microstructure. Careful control of the T_{max} value is needed to prevent the ductility being impaired.

The number of thermal cycles experienced determines the volume fraction, grain size and shape of primary α-phase—as well as the corresponding fineness of the α-phase laths within the transformed β-phase matrix. Raising the number of thermal cycles experienced by the material is serving further polarise the microstructure with ever larger primary α-phase grains and ever finer matrix α-phase grains.

Although variation of bimodal grain morphology was established by adjusting the heat treatment profile parameters, this

did not translate to a significant change in the tensile performance. However, it was shown that fine bimodal grains produced from a lower number of cycles demonstrated better fatigue performance compared to coarser grains produced by a high number of cycles.

The bimodal microstructures were out-performed in both tensile and high-cycle fatigue testing by a typical lamellar counterpart (sample treated at 950 °C for 2 h followed by an air cool). Although heat treatment cycling offers the tailoring of unique bimodal microstructure in printed Ti-6Al-4V components, more conventional annealing treatment strategies continue to offer superior mechanical performance.

Data availability

No data was used for the research described in the article.

Declaration of Competing Interest

The authors declare that they have no known competing financial interests or personal relationships that could have appeared to influence the work reported in this paper.

Acknowledgements

References

[1] S. Liu, Y.C. Shin, Additive manufacturing of Ti6Al4V alloy: A review, Mater. Des. 164 (Feb. 2019), https://doi.org/10.1016/j.matdes.2018.107552 107552.

[2] R. Narayan, Ed., ASM handbook. 23: Materials for medical devices / Roger J. Narayan … (vol.eds.). ASM International, Materials Park, Ohio, 2012.

[3] A. International, ASTM F3001-14: Standard Specification for Additive Manufacturing Titanium-6 Aluminum-4 Vanadium ELI (Extra Low Interstitial) with Powder Bed Fusion, 2014. [Online]. Available: www.astm.org.

[4] S. Cao et al., Role of martensite decomposition in tensile properties of selective laser melted Ti-6Al-4V, J. Alloys Compd. 744 (May 2018) 357–363, https://doi.org/10.1016/j.jallcom.2018.02.111.

[5] B. Vandenbroucke, J. Kruth, Selective laser melting of biocompatible metals for rapid manufacturing of medical parts, Rapid Prototyp. J. 13 (4) (Jan. 2007) 196–203, https://doi.org/10.1108/13552540710776142.

[6] L.E. Murr et al., Microstructure and mechanical behavior of Ti-6Al-4V produced by rapid-layer manufacturing, for biomedical applications, J. Mech. Behav. Biomed. Mater. 2 (1) (Jan. 2009) 20–32, https://doi.org/10.1016/j.jmbbm.2008.05.004.

[7] B. Vrancken, L. Thijs, J.-P. Kruth, J. Van Humbeeck, Heat treatment of Ti6Al4V produced by Selective Laser Melting: Microstructure and mechanical properties, J. Alloys Compd. 541 (Nov. 2012) 177–185, https://doi.org/10.1016/j.jallcom.2012.07.022.

[8] L. Facchini, E. Magalini, P. Robotti, A. Molinari, S. Höges, K. Wissenbach, Ductility of a Ti-6Al-4V alloy produced by selective laser melting of prealloyed powders, Rapid Prototyp. J. 16 (6) (Jan. 2010) 450–459, https://doi.org/10.1108/13552541011083371.

[9] T. Vilaro, C. Colin, J.D. Bartout, As-Fabricated and Heat-Treated Microstructures of the Ti-6Al-4V Alloy Processed by Selective Laser Melting, Metall. Mater. Trans. A 42 (10) (Oct. 2011) 3190–3199, https://doi.org/10.1007/s11661-011-0731-y.

[10] L. Thijs, F. Verhaeghe, T. Craeghs, J.V. Humbeeck, J.-P. Kruth, A study of the microstructural evolution during selective laser melting of Ti-6Al-4V, Acta Mater. 58 (9) (May 2010) 3303–3312, https://doi.org/10.1016/j.actamat.2010.02.004.

[11] G.J. Marshall, W.J. Young, S.M. Thompson, N. Shamsaei, S.R. Daniewicz, S. Shao, Understanding the Microstructure Formation of Ti-6Al-4V During Direct Laser Deposition via In-Situ Thermal Monitoring, JOM 68 (3) (Mar. 2016) 778–790, https://doi.org/10.1007/s11837-015-1767-z.

[12] P.A. Kobryn, S.L. Semiatin, The laser additive manufacture of Ti-6Al-4V, JOM 53 (9) (Sep. 2001) 40–42, https://doi.org/10.1007/s11837-001-0068-x.

[13] M. Simonelli, Y.Y. Tse, C. Tuck, Effect of the build orientation on the mechanical properties and fracture modes of SLM Ti-6Al-4V, Mater. Sci. Eng. A 616 (Oct. 2014) 1–11, https://doi.org/10.1016/j.msea.2014.07.086.

[14] S. Leuders et al., On the mechanical behaviour of titanium alloy TiAl6V4 manufactured by selective laser melting: Fatigue resistance and crack growth performance, Int. J. Fatigue 48 (Mar. 2013) 300–307, https://doi.org/10.1016/j.ijfatigue.2012.11.011.

[15] G. Kasperovich, J. Hausmann, Improvement of fatigue resistance and ductility of TiAl6V4 processed by selective laser melting, J. Mater. Process. Technol. 220 (Jun. 2015) 202–214, https://doi.org/10.1016/j.jmatprotec.2015.01.025.

[16] E. Sallica-Leva, R. Caram, A.L. Jardini, J.B. Fogagnolo, Ductility improvement due to martensite α′ decomposition in porous Ti-6Al-4V parts produced by selective laser melting for orthopedic implants, J. Mech. Behav. Biomed. Mater. 54 (Feb. 2016) 149–158, https://doi.org/10.1016/j.jmbbm.2015.09.020.

[17] A. Khorasani, I. Gibson, M. Goldberg, G. Littlefair, On the role of different annealing heat treatments on mechanical properties and microstructure of selective laser melted and conventional wrought Ti-6Al-4V, Rapid Prototyp. J. 23 (2) (Jan. 2017) 295–304, https://doi.org/10.1108/RPJ-02-2016-0022.

[18] C.V. Funch et al., Targeted heat treatment of additively manufactured Ti-6Al-4V for controlled formation of Bi-lamellar microstructures, J. Mater. Sci. Technol. 81 (Aug. 2021) 67–76, https://doi.org/10.1016/j.jmst.2021.01.004.

[19] R. Sabban, S. Bahl, K. Chatterjee, S. Suwas, Globularization using heat treatment in additively manufactured Ti-6Al-4V for high strength and toughness, Acta Mater. 162 (Jan. 2019) 239–254, https://doi.org/10.1016/j.actamat.2018.09.064.

[20] H. Bai, et al., Effect of Heat Treatment on the Microstructure and Mechanical Properties of Selective Laser-Melted Ti64 and Ti-5Al-5Mo-5V-1Cr-1Fe, Metals 11(4), Art. no. 4, Apr. 2021, doi: 10.3390/met11040534.

[21] C.-L. Li et al., Realizing superior ductility of selective laser melted Ti-6Al-4V through a multi-step heat treatment, Mater. Sci. Eng. A 799 (Jan. 2021), https://doi.org/10.1016/j.msea.2020.140367 140367.

[22] J.A. Hines, G. Lütjering, Propagation of microcracks at stress amplitudes below the conventional fatigue limit in Ti-6Al-4V, Fatigue Fract. Eng. Mater. Struct. 22 (8) (1999) 657–665, https://doi.org/10.1046/j.1460-2695.1999.t01-1-00217.x.

[23] R.K. Nalla, B.L. Boyce, J.P. Campbell, J.O. Peters, R.O. Ritchie, Influence of microstructure on high-cycle fatigue of Ti-6Al-4V: Bimodal vs. lamellar structures, Metall. Mater. Trans. A, p. 20.

[24] J.H. Zuo, Z.G. Wang, E.H. Han, Effect of microstructure on ultra-high cycle fatigue behavior of Ti-6Al-4V, Mater. Sci. Eng. A 473 (1) (Jan. 2008) 147–152, https://doi.org/10.1016/j.msea.2007.04.062.

[25] G.Q. Wu, C.L. Shi, W. Sha, A.X. Sha, H.R. Jiang, Effect of microstructure on the fatigue properties of Ti-6Al-4V titanium alloys, Mater. Des. 46 (Apr. 2013) 668–674, https://doi.org/10.1016/j.matdes.2012.10.059.

[26] V. Crupi, G. Epasto, E. Guglielmino, A. Squillace, Influence of microstructure [alpha+beta and beta] on very high cycle fatigue behaviour of Ti-6Al-4V alloy, Int. J. Fatigue 95 (Feb. 2017) 64–75, https://doi.org/10.1016/j.ijfatigue.2016.10.002.

[27] C. Huang et al., Ductilization of selective laser melted Ti6Al4V alloy by friction stir processing, Mater. Sci. Eng. A 755 (May 2019) 85–96, https://doi.org/10.1016/j.msea.2019.03.133.

[28] S. Leuders, On the fatigue properties of metals manufactured by selective laser melting-the role of ductility, J. Mater. Res. (2014).

[29] H.M. Rietveld, A profile refinement method for nuclear and magnetic structures, J. Appl. Crystallogr. 2(2), Art. no. 2, Jun. 1969, doi: 10.1107/S0021889869006558.

[30] L. Lutterotti, MAUD (material analysis using diffraction): a user friendly Java program for Rietveld texture analysis and more, in: Proceeding of the twelfth international conference on textures of materials (ICOTOM-12), Ottowa, Canada, 1999, vol. Vol. 1.

[31] H.C. Kaushik, M.H. Korayem, A. Hadadzadeh, Determination of α to β phase transformation kinetics in laser-powder bed fused Ti-6Al-2Sn-4Zr-2Mo-0.08Si and Ti-6Al-4V alloys, Mater. Sci. Eng. A 860 (Dec. 2022), https://doi.org/10.1016/j.msea.2022.144294 144294.

[32] X.-Y. Zhang, G. Fang, S. Leeflang, A.J. Böttger, A.A. Zadpoor, J. Zhou, Effect of subtransus heat treatment on the microstructure and mechanical properties of additively manufactured Ti-6Al-4V alloy, J. Alloys Compd. 735 (Feb. 2018) 1562–1575, https://doi.org/10.1016/j.jallcom.2017.11.263.

[33] N. Saunders, Modelling of phase equilibria in Ti-alloys," presented at the Titanium'95- Science and technology, 1996, pp. 2167–2176.

[34] C. Liu, Y. Lu, X. Tian, D. Liu, Influence of continuous grain boundary α on ductility of laser melting deposited titanium alloys, Mater. Sci. Eng. A 661 (Apr. 2016) 145–151, https://doi.org/10.1016/j.msea.2016.03.034.

[35] J. Sieniawski and W. Ziaja, Titanium Alloys: Advances in Properties Control. BoD – Books on Demand, 2013.

[36] G. Lütjering, J.C. Williams, Titanium, 2nd ed., Springer, Berlin; New York, 2007.

[37] J. Günther et al., Fatigue life of additively manufactured Ti-6Al-4V in the very high cycle fatigue regime, Int. J. Fatigue 94 (Jan. 2017) 236–245, https://doi.org/10.1016/j.ijfatigue.2016.05.018.

[38] J. Xi, et al., The Low-Cycle Fatigue Behavior, Failure Mechanism and Prediction of SLM Ti-6Al-4V Alloy with Different Heat Treatment Methods, Materials, vol. 14, no. 21, Art. no. 21, Jan. 2021, doi: 10.3390/ma14216276.

[39] M. Qian, W. Xu, M. Brandt, H.P. Tang, Additive manufacturing and postprocessing of Ti-6Al-4V for superior mechanical properties, MRS Bull. 41 (10) (Oct. 2016) 775–784, https://doi.org/10.1557/mrs.2016.215.

[40] E. Wycisk, A. Solbach, S. Siddique, D. Herzog, F. Walther, C. Emmelmann, Effects of Defects in Laser Additive Manufactured Ti-6Al-4V on Fatigue Properties, Phys. Procedia 56 (Jan. 2014) 371–378, https://doi.org/10.1016/j.phpro.2014.08.120.

[41] H.K. Rafi, N.V. Karthik, H. Gong, T.L. Starr, B.E. Stucker, Microstructures and Mechanical Properties of Ti6Al4V Parts Fabricated by Selective Laser Melting and Electron Beam Melting, J. Mater. Eng. Perform. 22 (12) (Dec. 2013) 3872–3883, https://doi.org/10.1007/s11665-013-0658-0.

[42] T. Mishurova et al., Separation of the impact of residual stress and microstructure on the fatigue performance of LPBF Ti-6Al-4V at elevated temperature, Int. J. Fatigue 148 (Jul. 2021), https://doi.org/10.1016/j.ijfatigue.2021.106239 106239.

[43] T. Mishurova, et al., An Assessment of Subsurface Residual Stress Analysis in SLM Ti-6Al-4V, Materials vol. 10, no. 4, Art. no. 4, Apr. 2017, doi: 10.3390/ma10040348.

[44] S. Li, B. Xiong, S. Hui, W. Ye, Y. Yu, Comparison of the fatigue and fracture of Ti–6Al–2Zr–1Mo–1V with lamellar and bimodal microstructures, Mater. Sci. Eng. A 460–461 (Jul. 2007) 140–145, https://doi.org/10.1016/j.msea.2007.02.064.

[45] C. Tan, Q. Sun, G. Zhang, Y. Zhao, High-cycle fatigue of a titanium alloy: the role of microstructure in slip irreversibility and crack initiation, J. Mater. Sci. 55 (26) (Sep. 2020) 12476–12487, https://doi.org/10.1007/s10853-020-04845-7.

[46] J.H. Rao, N. Stanford, A survey of fatigue properties from wrought and additively manufactured Ti-6Al-4V, Mater. Lett. 283 (Jan. 2021), https://doi.org/10.1016/j.matlet.2020.128800 128800.